Myosin IIA interacts with the spectrin-actin membrane skeleton to control red blood cell membrane curvature and deformability

Alyson S. Smith[a,1], Roberta B. Nowak[a,1], Sitong Zhou[b,c,d], Michael Giannetto[b,c,d], David S. Gokhin[a], Julien Papoin[e], Ionita C. Ghiran[f], Lionel Blanc[e,g,h], Jiandi Wan[b,c,d], and Velia M. Fowler[a,2]

[a]Department of Molecular Medicine, The Scripps Research Institute, La Jolla, CA 92037; [b]Microsystems Engineering, Rochester Institute of Technology, Rochester, NY 14623; [c]Department of Biomedical Engineering, University of Rochester, Rochester, NY 14623; [d]Center for Translational Neuromedicine, University of Rochester Medical Center, Rochester, NY 14623; [e]Center for Autoimmune, Musculoskeletal and Hematopoietic Diseases, The Feinstein Institute for Medical Research, Manhasset, NY 11030; [f]Department of Medicine, Beth Israel Deaconess Medical Center, Boston, MA 02115; [g]Department of Molecular Medicine, Donald and Barbara Zucker School of Medicine at Hofstra/Northwell, Hempstead, NY 11030; and [h]Department of Pediatrics, Donald and Barbara Zucker School of Medicine at Hofstra/Northwell, Hempstead, NY 11030

Edited by Vann Bennett, Duke University Medical Center, Durham, NC, and approved March 14, 2018 (received for review October 19, 2017)

The biconcave disk shape and deformability of mammalian RBCs rely on the membrane skeleton, a viscoelastic network of short, membrane-associated actin filaments (F-actin) cross-linked by long, flexible spectrin tetramers. Nonmuscle myosin II (NMII) motors exert force on diverse F-actin networks to control cell shapes, but a function for NMII contractility in the 2D spectrin–F-actin network of RBCs has not been tested. Here, we show that RBCs contain membrane skeleton-associated NMIIA puncta, identified as bipolar filaments by superresolution fluorescence microscopy. MgATP disrupts NMIIA association with the membrane skeleton, consistent with NMIIA motor domains binding to membrane skeleton F-actin and contributing to membrane mechanical properties. In addition, the phosphorylation of the RBC NMIIA heavy and light chains in vivo indicates active regulation of NMIIA motor activity and filament assembly, while reduced heavy chain phosphorylation of membrane skeleton-associated NMIIA indicates assembly of stable filaments at the membrane. Treatment of RBCs with blebbistatin, an inhibitor of NMII motor activity, decreases the number of NMIIA filaments associated with the membrane and enhances local, nanoscale membrane oscillations, suggesting decreased membrane tension. Blebbistatin-treated RBCs also exhibit elongated shapes, loss of membrane curvature, and enhanced deformability, indicating a role for NMIIA contractility in promoting membrane stiffness and maintaining RBC biconcave disk cell shape. As structures similar to the RBC membrane skeleton exist in many metazoan cell types, these data demonstrate a general function for NMII in controlling specialized membrane morphology and mechanical properties through contractile interactions with short F-actin in spectrin–F-actin networks.

actomyosin contractility | cytoskeleton | erythrocyte deformability | cell shape | TIRF microscopy

RBC biconcave disk shape and deformability provide a maximal surface-area-to-volume ratio for optimal gas and ion exchange and enable repeated transit through blood vessels less than half their diameter during the ∼120-day RBC lifespan (1–3). Appropriate levels of RBC deformation also regulate blood flow and oxygen delivery via mechanotransductive pathways that release ATP to induce vasodilation and hyperemia (4). These properties all rely upon the membrane skeleton, a 2D quasihexagonal network of short (∼37 nm) actin filament (F-actin) nodes interconnected by ∼200-nm-long, flexible $(\alpha_1\beta_1)_2$-spectrin tetramers (5, 6). Molecular genetics, biochemistry, biophysics, and physiology of human and mouse congenital hemolytic anemias have shown that multiple proteins, which mediate the connectivity of the micrometer-scale 2D network and the network's multipoint attachments to the membrane, are critical for RBC shape and deformability (1, 2, 5, 7). Similar spectrin–F-actin networks are a conserved feature of metazoan cells, where they create specialized membrane domains of ion channels, pumps, or cell adhesion molecules that confer complex signaling, cell interactions, and mechanical resilience to the plasma membrane (8–10).

Although researchers first documented the biconcave disk shape of RBCs nearly 200 years ago (11), numerous unanswered questions remain regarding the forces that generate and maintain this unique cellular morphology (5, 12, 13). Nonmuscle myosin II (NMII), a force-generating motor protein identified and purified from RBCs >30 years ago, forms heterohexamers (termed NMII molecules) of two heavy chains (HC), two regulatory light chains (RLC), and two essential light chains (14, 15). In vitro experiments show that, similar to NMII from other cells, RBC NMII molecules have F-actin–activated MgATPase activity regulated by myosin light chain kinase (MLCK) phosphorylation of the RLC and can assemble into bipolar filaments with motor domains at filament ends (14–16). Each mature human RBC contains ∼6,200 NMII molecules and ∼500,000 actin molecules, resulting in about 80 actin molecules per NMII molecule, similar to the ratio in other cells, such as platelets (15–17). NMII in mature RBCs has been hypothesized to control RBC shapes (15,

Significance

The biconcave disk shape and deformability of the mammalian RBC are vital to its circulatory function and rely upon a 2D viscoelastic spectrin–F-actin network attached to the membrane. A role for nonmuscle myosin II (NMII) contractility in generating tension in this network and controlling RBC shape has not been tested. We show that NMIIA forms bipolar filaments in RBCs, which associate with F-actin at the membrane. NMIIA motor activity regulates interactions with the spectrin–F-actin network to control RBC biconcave shape and deformability. These results provide a previously undescribed mechanism for actomyosin force generation at the plasma membrane, and may apply to spectrin–F-actin–based membrane skeleton networks in other cell types, such as neurons and polarized epithelial cells.

Author contributions: A.S.S., R.B.N., I.C.G., L.B., J.W., and V.M.F. designed research; A.S.S., R.B.N., S.Z., M.G., D.S.G., J.P., I.C.G., and V.M.F. performed research; A.S.S., R.B.N., S.Z., D.S.G., I.C.G., L.B., J.W., and V.M.F. analyzed data; and A.S.S., L.B., J.W., and V.M.F. wrote the paper.

The authors declare no conflict of interest.

This article is a PNAS Direct Submission.

[1]A.S.S. and R.B.N. contributed equally to this work.

[2]To whom correspondence should be addressed. Email: velia@scripps.edu.

This article contains supporting information online at www.pnas.org/lookup/suppl/doi:10.1073/pnas.1718285115/-/DCSupplemental.

18, 19), repair local disruptions in the spectrin–F-actin network (20), or remain as a nonfunctional vestige from an earlier and more motile stage of erythroblast terminal differentiation and maturation (17), but none of these hypotheses have been experimentally tested.

In most nucleated eukaryotic cells, NMII bipolar filaments generate tension to control membrane deformations and cell shape by pulling on F-actin in the cortex, a thick, irregular, 3D network of relatively long (100–600 nm) actin filaments adjacent to the plasma membrane (21–24). By contrast, the RBC membrane skeleton is a thin, regular, 2D spectrin–F-actin network that underlies the membrane and consists of much shorter (~37 nm) actin filaments that bind a unique complement of proteins (25). Because of these differences in geometry and composition, it is an open question whether NMII can pull on the short F-actin of the RBC membrane skeleton, or the membrane skeleton networks of other metazoan cells, to generate tension and influence membrane properties, such as curvature and mechanics. RBCs are an ideal model system to test this question, as RBC F-actin is present exclusively in the membrane

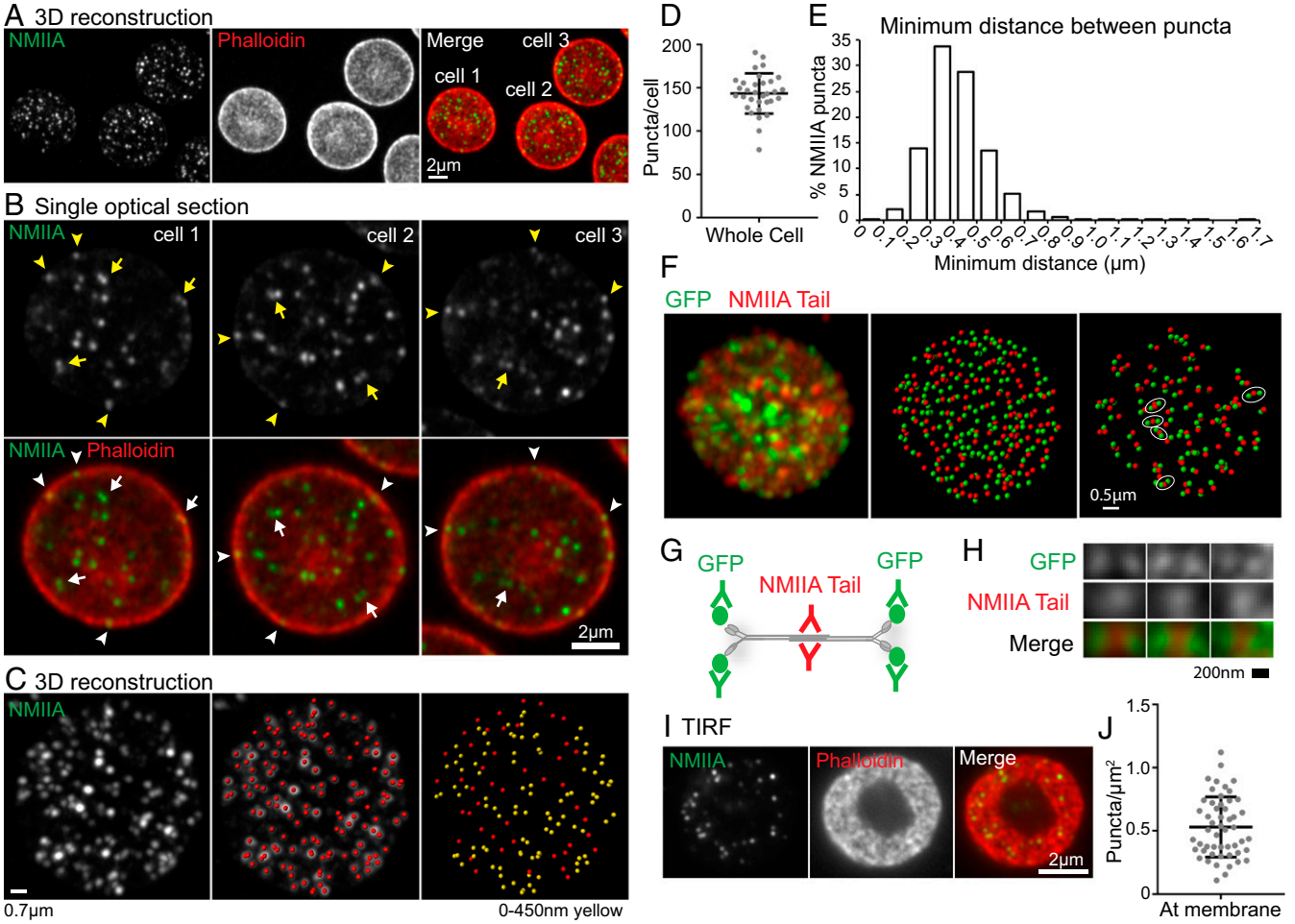

Fig. 1. NMIIA localizes as puncta, which likely represent bipolar filaments, throughout each RBC. (*A*) Three-dimensional reconstruction of a superresolution AiryScan confocal Z-stack of human RBCs immunostained with an antibody to the motor domain of NMIIA (green) and rhodamine-phalloidin for F-actin (red). (*B*) Higher magnification views of NMIIA motor domain puncta in single XY optical sections from the superresolution AiryScan Z-stack shown in *A*, showing some puncta at the membrane (arrowheads) and some closely spaced doublets of puncta (arrows). (*C*, *Left*) Three-dimensional reconstruction of a representative human RBC stained for NMIIA. (*C*, *Center*) Image shows NMIIA puncta computationally identified in Imaris (red dots) superimposed on the NMIIA staining (grayscale). (*C*, *Right*) Image shows computationally identified NMIIA puncta alone. Identified puncta are color-coded based on the minimum distance to the nearest punctum in three dimensions, with yellow dots representing puncta ≤450 nm from the nearest neighboring punctum and red dots representing puncta >450 nm from the nearest neighboring puncta. (*D*) Quantification of the number of NMIIA puncta per cell from 3D AiryScan images. Numbers were calculated by dividing the total number of puncta in each image by the number of cells in each image ($n = 32$ images; 176 total cells from two individual donors). Mean ± SD = 143 ± 23 puncta per cell. (*E*) Histogram showing distribution of the minimum distances between NMIIA motor domain puncta measured from AiryScan images of whole RBCs similar to those in *A*–*C* ($n = 25{,}067$ puncta from 176 cells from two individual donors). Mean ± SD = 0.42 ± 0.13 μm apart. Sixty-six percent of puncta are between 200 and 450 nm apart. (*F*, *Left*) Image shows 3D reconstruction of a superresolution AiryScan Z-stack of a mouse RBC expressing NMIIA tagged with GFP on the N terminus stained with an antibody against GFP (green) and the NMIIA tail (red). (*F*, *Center*) Image shows puncta computationally identified in Imaris from both channels. (*F*, *Right*) Image shows only the puncta that are ≤250 nm from another punctum in either channel. Groups with one NMIIA tail punctum between two GFP puncta, representing stained NMIIA bipolar filaments, are circled. (*G*) Diagram showing the epitopes of the antibodies used in *H* and representing the stained triplets of puncta observed. (*H*) High-magnification examples of GFP-tail-GFP puncta triplets observed in *G*. (*I*) TIRF microscopy images of immunostaining for the NMIIA motor domain (green) and rhodamine phalloidin for F-actin (red) in human RBCs showing an *en face* view of the membrane surface within 100–200 nm of the coverslip. (*J*) Quantification of the density of NMIIA puncta per square micrometer within 200 nm of the membrane from TIRF images ($n = 52$ RBCs from two individual donors). Lines represent mean ± SD (0.53 ± 0.24 puncta per square micrometer).

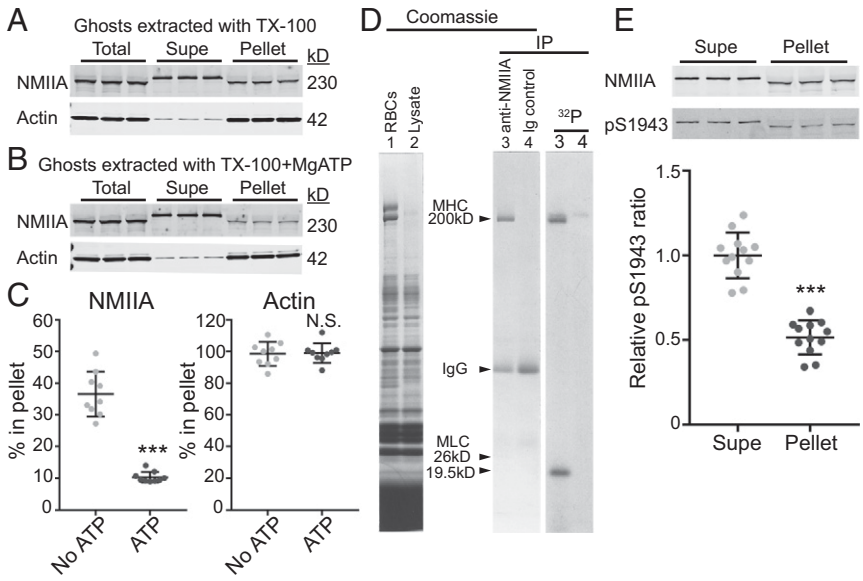

Fig. 2. NMIIA association with the RBC membrane skeleton is MgATP-dependent, and NMIIA HC and RLC phosphorylation indicates active regulation of NMIIA motor activity and filament assembly at the membrane skeleton. Human RBC Mg^{2+} ghosts were extracted in TX-100 buffer without (*A*) or with (*B*) addition of 5 mM MgATP, followed by SDS/PAGE and immunoblotting for NMIIA HC or actin in the soluble (Supe) and insoluble membrane skeleton (Pellet) fractions. The decreased mobility for the NMII HC in ghosts and TX-100–extracted pellet samples on these acrylamide gradient minigels is due to the large excess of spectrin over NMIIA HC, which forces the HC to migrate faster and is not observed on large-format, low-percentage gels (Fig. S3). (*C*) Quantification of the percentage of NMIIA or actin in the membrane skeleton fraction. A portion of NMIIA (36.5 ± 7.1%) is in the TX-100–insoluble pellet in the absence of MgATP, and 10.4 ± 1.7% is in the pellet in the presence of MgATP (***$P < 0.0001$). Most of the actin (98.5 ± 7.5%) is in the TX-100–insoluble pellet with no ATP, and 98.9 ± 6.25% is in the pellet with ATP. Each point represents one of three technical replicates for each of three biological replicates (ghosts from three donors), for a total $n = 9$. Lines represent mean ± SD. N.S., not significant. (*D*) Live human RBCs were metabolically labeled with ^{32}P-orthophosphate to detect phosphorylated proteins and lysed, and native NMIIA was immunoprecipitated under nondenaturing conditions. (*Left*) Coomassie Blue gel of total RBCs (lane 1) and lysate before immunoprecipitation (IP; lane 2). (*Right*) Coomassie Blue gel of anti-NMIIA IP (lane 3) and preimmune IgG IP (lane 4), and autoradiogram of this gel. The RBC NMIIA 26-kD essential light chain and 19.5-kD RLC were visible in the original Coomassie-stained gel but faded upon destaining (15). (*E*) Human RBC Mg^{2+} ghosts were extracted in TX-100 buffer, followed by SDS/PAGE and immunoblotting for NMIIA HC (*Top*) or NMIIA HC phosphorylated on serine 1943 (pS1943; *Bottom*). Quantification shows that the ratio of pS1943 HC/total HC is about twofold higher in the TX-100–soluble supernatant (mean ± SD = 1.0 ± 0.13) compared with the TX-100–insoluble pellet (mean ± SD = 0.52 ± 0.10). Each point represents one of three technical replicates for each of four biological replicates (four individual donors), for a total $n = 12$ (***$P < 0.0001$). Lines represent mean ± SD.

skeleton, obviating confounding contributions from other F-actin populations (5, 6).

In this study, we provide evidence that NMIIA is the predominant RBC NMII isoform. Superresolution and total internal reflection fluorescence (TIRF) microscopy indicate that NMIIA can form bipolar filaments in intact RBCs, and that some filaments associate with membrane skeleton F-actin. Biochemical assays show that binding of NMIIA motor domains to F-actin mediates this membrane association. Moreover, in vivo phosphorylation of the RBC NMIIA HC and RLC demonstrates active regulation of NMIIA motor activity and filament assembly. Inhibition of NMIIA contractility with blebbistatin results in reduced NMIIA association with the membrane, RBC elongation and loss of biconcavity, and increased local and global membrane deformability. These results demonstrate a previously unrealized motor-dependent interaction between NMIIA and the spectrin–F-actin membrane skeleton that controls RBC membrane tension, biconcave disk shape, and deformability.

Results

NMIIA, the Predominant NMII Isoform in Human RBCs, Forms Bipolar Filaments at the RBC Membrane. The majority of cell types express more than one isoform of the NMII HC, typically the NMIIA HC encoded by the *MYH9* gene and the NMIIB HC encoded by the *MYH10* gene (22–24). A third NMIIC HC isoform, encoded by the *MYH14* gene, is also present in some cell types but is not as widely expressed as the *MYH9* and *MYH10* genes (26). To assess NMII isoform content during human erythroid differentiation, we induced human $CD34^+$ cells to differentiate into erythroid cells in vitro (Fig. S1*A*). Quantitative real-time PCR (qRT-PCR) confirms previous microarray and RNA-sequencing analysis (27, 28), showing that early stages of erythroid culture express *MYH9* and *MYH10* transcripts, which decrease during the final stages of terminal erythroid maturation (Fig. S1*B*).

Immunoblots of the same samples show that NMIIB HC protein decreases below detectable levels by day 10 of differentiation, while NMIIA HC protein persists through day 16 of culture (Fig. S1*C*), when most erythroblasts have extruded their nuclei to become reticulocytes, as shown in Fig. S1*A*. This extends a previous analysis of NMII HC isoform protein expression in earlier stages of erythroid culture (29). Immunoblotting of human RBC membranes (ghosts) isolated by hypotonic hemolysis further indicates that NMIIA is the predominant NMII isoform in mature human RBCs (Fig. S1*D*). These data agree with previous 2D chymotryptic peptide maps, which are nearly identical for purified RBC NMII HC and platelet NMIIA HC (15).

To characterize the distribution of NMIIA in RBCs, we immunostained fixed, biconcave RBCs for the NMIIA motor domain and stained F-actin with phalloidin. The low abundance of NMIIA in RBCs [~6,200 molecules per cell (5, 17)], the high concentration of fluorescence-quenching hemoglobin (30), and the small sizes of RBCs [8 μm in diameter × 2 μm thick (31)] make imaging RBC NMIIA challenging. Therefore, we imaged RBCs using sensitive, superresolution AiryScan confocal fluorescence microscopy (32). Three-dimensional reconstructions of Z-stacks revealed ~150 NMIIA motor domain puncta distributed throughout each RBC, distinct from the more continuous F-actin localization at the membrane (Fig. 1 *A* and *D*). Single

optical sections of individual RBCs showed NMIIA motor domain puncta throughout the RBC and at the edge of the RBC, localized with F-actin at the membrane (Fig. 1*B*, arrowheads).

We identified doublets of NMIIA motor domain puncta spaced 200–450 nm apart (Fig. 1*B*, arrows), similar to the lengths of NMIIA bipolar filaments observed in vitro and in other cells using electron and superresolution microscopy (33–38). Three-dimensional nearest neighbor analysis showed that ∼66% of NMIIA motor domain puncta form closely spaced doublets with one other punctum, which suggests that these doublets could represent NMIIA bipolar filaments (Fig. 1 *C*, yellow dots and *E*). To provide further evidence for the presence of NMIIA filaments in RBCs, we immunostained RBCs from mice expressing NMIIA tagged with GFP at the motor domain (39) with antibodies to GFP and the NMIIA tail domain (Fig. 1*F*). In these cells, we observed groups of puncta with one tail domain punctum between two GFP (motor domain) puncta (Fig. 1*G*), representing immunostained NMIIA bipolar filaments (Fig. 1*H*). Closely spaced pairs of motor and tail domain puncta and isolated single puncta may represent small, immature bipolar filaments below the resolution of AiryScan, unipolar NMIIA filaments (40), or bipolar NMIIA filaments not stained efficiently enough to be detected and resolved.

To examine NMIIA motor domain association with F-actin at the membrane, we performed TIRF microscopy, which selectively illuminates fluorophores located within 100–200 nm from the coverslip, at or near the plasma membrane (41). TIRF images of F-actin in biconcave RBCs reveal a donut-shaped appearance where the membrane of the rim is in close contact with the coverslip (Fig. 1*I* and Fig. S2*A*). Discrete NMIIA motor domain puncta appear scattered throughout this donut-shaped region, localizing with F-actin at the membrane at an average density of ∼0.5 puncta per square micrometer (Fig. 1 *I* and *J* and Fig. S2*A*), and are absent from secondary antibody-alone controls (Fig. S2*A*). Based on a total RBC surface area of 140 μm^2 (42), these data show that ∼70 NMIIA puncta are associated with the membrane of each RBC. RBCs stained with an antibody to the NMIIA tail domain (Fig. S2 *B–D*) or polyclonal antibodies to NMIIA (15) display similar patterns and numbers of NMIIA puncta to those stained with the antibody to the motor domain. This is likely because the 2D epifluorescence and TIRF images are unable to resolve closely spaced doublets of motor domain puncta not parallel to the plane of the membrane, unlike the 3D AiryScan images.

ATP Disrupts NMIIA Association with the Triton X-100–Insoluble Membrane Skeleton. A contractile function for NMIIA bipolar filaments in RBCs should involve interactions of NMIIA motor domains with F-actin in the membrane skeleton (22–24). In vitro biochemical and biophysical studies show that MgATP weakens purified NMII motor domain binding to F-actin as part of the NMII catalytic cycle (43). To test whether MgATP disrupts RBC NMIIA association with F-actin, we isolated membrane skeletons by extracting RBC membranes (Mg^{2+} ghosts) with Triton X-100 (TX-100) to solubilize lipids and transmembrane proteins and to remove any remaining cytosolic components (15, 44) (Fig. 2 *A* and *B*). In the absence of MgATP, ∼40% of the NMIIA HC in Mg^{2+} ghosts is associated with the Triton-insoluble membrane skeleton pellet (Fig. 2 *A* and *C*). Addition of MgATP to the Triton lysis buffer disrupted this association, decreasing the percentage of pellet-associated NMIIA to 10% (Fig. 2 *B* and *C*). In agreement with these results, depletion of endogenous ATP with hexokinase and glucose in Triton lysate prepared from whole RBCs increased the levels of NMIIA associated with the Triton-insoluble membrane skeleton pellet (Fig. S3 *B* and *C*).

By contrast, nearly all of the actin is associated with the membrane skeleton in both the absence and presence of MgATP (Fig. 2 *A–C*). In both conditions, all of the spectrin and other membrane skeleton proteins are present in the Triton-insoluble pellet, as described previously (44, 45), while a significant fraction of band 3, a major integral membrane protein (100 kD), is extracted into the supernatant, as expected (Fig. S3*A*). Thus, the disruption of NMIIA association with the membrane skeleton by MgATP is not due to selective extraction of actin or other membrane skeleton proteins. These data show that NMIIA associates more stably with the membrane skeleton in the absence of MgATP, suggesting that NMIIA associates with the RBC membrane skeleton via motor domain binding to F-actin.

Phosphorylation of the RBC NMIIA HC and RLC Is Consistent with Contractility and Regulated Filament Assembly. Signaling pathways that phosphorylate multiple sites of the NMII HC and RLC regulate NMII motor activity and filament assembly (22–24, 46). To determine whether RBC NMIIA HC or RLC is phosphorylated in vivo, we metabolically labeled RBCs with ^{32}P orthophosphate and then immunoprecipitated native NMIIA under conditions that preserve HC-LC associations. SDS/PAGE and autoradiography revealed that both the 19.5-kDa RLC and the HC are phosphorylated (Fig. 2*D*). To test whether NMIIA HC phosphorylation status affects association with the membrane skeleton, we extracted Mg^{2+}

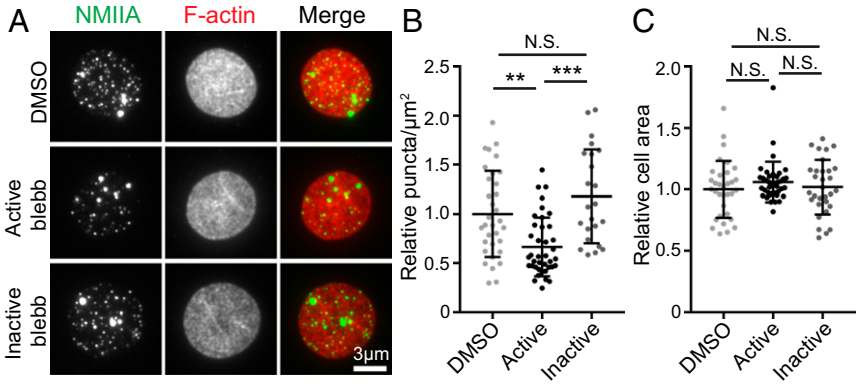

Fig. 3. NMIIA motor activity controls the association of NMIIA puncta with the RBC membrane. (*A*) TIRF microscopy of NMIIA motor domain (green) and rhodamine-phalloidin for F-actin (red) in human RBCs pretreated with DMSO alone, 20 μM active blebbistatin (blebb), or 20 μM inactive blebb before fixation and immunostaining. RBCs were flattened by centrifugation onto glass coverslips before imaging to visualize a larger area of the membrane. (*B*) NMIIA puncta density at the RBC membrane measured as the number of NMIIA puncta per square micrometer in TIRF images. DMSO versus active blebbistatin (**$P = 0.0016$) and active blebbistatin versus inactive blebbistatin (***$P < 0.0001$) are shown. (*C*) Cell surface areas for RBCs in TIRF images in each treatment group. There is no significant difference in cell areas between treatment groups by one-way ANOVA. Cells from two individual donors are shown: DMSO ($n = 33$), active blebbistatin ($n = 40$), and inactive blebbistatin ($n = 31$). N.S., not significant.

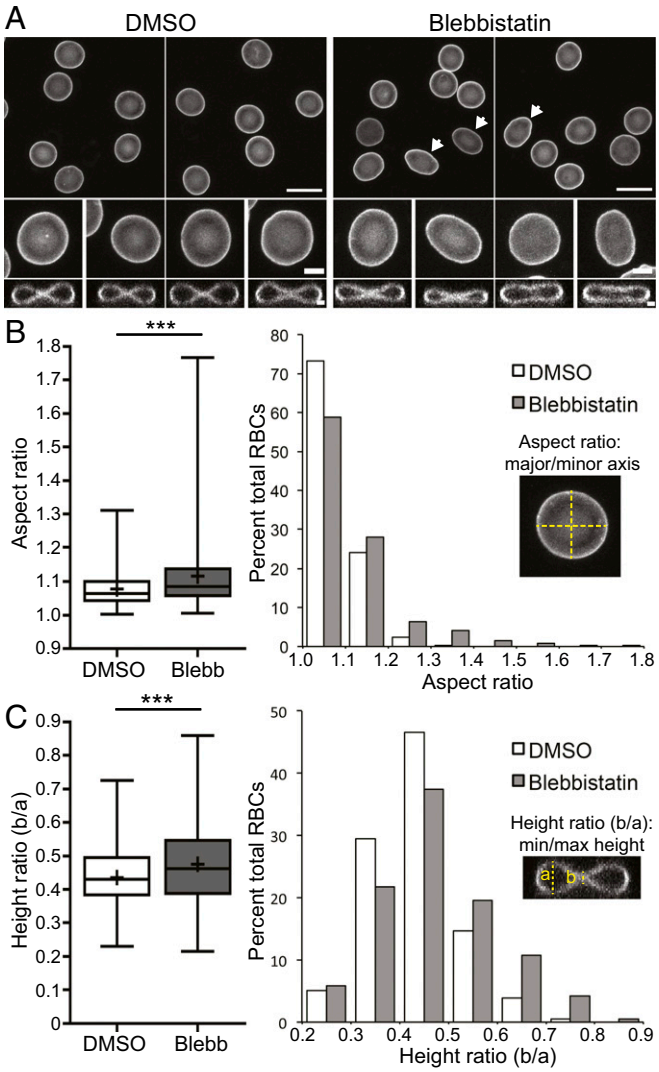

Fig. 4. NMIIA motor activity controls RBC morphology. (*A*) Confocal fluorescence microscopy images of glycophorin A-stained RBCs after treatment with DMSO or 20 μM active blebbistatin. XY maximum intensity projections (*Top* and *Middle*) and XZ slices from the middle of the cell (*Bottom*) are shown. (Scale bars: *Top*, 10 μm; *Middle*, 2 μm; *Bottom*, 1 μm). DMSO-treated control RBCs are round in XY and biconcave in XZ views, as expected. Note elongated cells (arrows) and cells with relaxed dimples after treatment with blebbistatin. (*B*) RBC elongation measured from aspect ratios (major/minor axis) in XY maximum intensity projections as in *A*. A box-and-whisker plot (*Left*) and histogram (*Right*) are shown. DMSO versus blebbistatin (Blebb) (***$P < 0.0001$) is shown. Variances were significantly different by *F*-test (***$P < 0.0001$). (*C*) RBC biconcavity measured from the ratio of cell height at the dimple to the height at the rim from XZ slices as in *A*. A box-and-whisker plot (*Left*) and histogram (*Right*) are shown. DMSO versus Blebb (***$P < 0.0001$) is shown. Variances were significantly different by *F*-test (***$P < 0.001$). For box-and-whisker plots, the middle line represents the median; upper and lower lines represent the third and first quartiles, respectively; and whiskers represent minimum and maximum values. Plus symbols denote means. Cells are shown for the following: DMSO [$n = 423$ RBCs (four donors)] and blebbistatin [$n = 410$ RBCs (four donors)].

ghosts in TX-100 as described above. We found that the ratio of NMIIA HC phosphorylated at serine 1943 to the total HC was about twofold greater in the Triton-soluble supernatant compared with the Triton-insoluble membrane skeleton pellet (Fig. 2*E*). As HC phosphorylation at this residue inhibits filament assembly and promotes filament turnover (46), this suggests that membrane skeleton-associated NMIIA filaments have reduced HC phosphorylation and increased stability.

NMIIA Motor Activity Controls NMIIA Association with the RBC Membrane. Functional interactions of NMIIA filaments with F-actin in the RBC membrane skeleton should depend on motor domain activity, which may affect NMIIA and F-actin distribution at the RBC membrane. Therefore, we treated live, intact RBCs with blebbistatin, an NMII-specific motor inhibitor that prevents phosphate release and stalls NMII in a weak F-actin–binding state (43). We evaluated NMIIA association with the membrane by TIRF microscopy of fixed RBCs immunostained for the NMIIA motor domain and flattened by centrifugation onto glass coverslips before imaging to provide a greater membrane surface area to examine (Fig. 3*A*). Blebbistatin treatment of RBCs resulted in an ∼30% reduction in NMIIA puncta density at the membrane relative to DMSO treatment, while the inactive blebbistatin enantiomer had no significant effect (Fig. 3*B*). The change in NMIIA puncta density was not due to changes in the extent of RBC flattening, since blebbistatin treatment had no effect on the area of RBC F-actin visualized by TIRF microscopy (Fig. 3*C*).

To determine whether inhibition of NMIIA motor activity affects the organization of membrane skeleton F-actin, we examined TIRF images of phalloidin-stained RBCs treated with DMSO, active blebbistatin, or inactive blebbistatin. F-actin appeared as a dense, reticular network, with no detectable differences in organization across all three treatment groups (Fig. S4*A*). In addition, treatment with active blebbistatin did not affect levels of G-actin in the cytosol, indicating that global F-actin stability was not altered (Fig. S4 *B* and *C*). Together, these data indicate that inhibition of NMIIA motor activity in RBCs affects the localization of NMIIA at the membrane but does not lead to global rearrangements or disassembly of the spectrin–F-actin membrane skeleton.

NMIIA Motor Activity Controls RBC Morphology. Through attachments to transmembrane proteins, the RBC membrane skeleton provides appropriate levels of membrane tension to maintain biconcave shape (1, 2, 7). Because blebbistatin inhibition of NMIIA motor activity reduced NMIIA membrane association, we predicted that blebbistatin treatment would lead to a loss in membrane tension and changes in RBC membrane curvature and shape. To test this hypothesis, we evaluated RBC shapes in 3D confocal images after immunostaining for glycophorin A, a membrane marker (Fig. 4*A*). Treatment with 20 μM active blebbistatin caused RBCs to variably elongate compared with the DMSO control, measured as an increased mean and variance of the aspect ratio (major/minor axis) in XY maximum intensity projections (Fig. 4*B*). Blebbistatin treatment also caused a variable loss of biconcavity, measured as an increased mean and variance of the height ratio (minimum/maximum height) of XZ slices from the center of each RBC (Fig. 4*C*). Treatment with the inactive blebbistatin enantiomer did not affect RBC aspect ratio or biconcavity, and increasing the concentration of active blebbistatin to 50 μM did not lead to further changes in either parameter (Fig. S5).

We conclude that NMIIA motor activity maintains the membrane curvature required for the characteristic RBC biconcave shape. We found a positive correlation between the extent of elongation and biconcavity in RBCs treated with DMSO and active blebbistatin; however, these parameters varied independently in many cells, reducing the extent of this relationship (Fig. S6*A*). In addition, changes in biconcavity arose within 30 min of active blebbistatin treatment, but significant changes in the aspect ratio did not appear until after 2 h of treatment (Fig. S6 *B* and *C*). These data suggest that RBC aspect ratio and biconcavity may depend on different aspects of NMIIA motor activity.

To determine whether known NMIIA RLC kinases (22–24) regulate NMII contractility to control RBC shape, we treated human RBCs with kinase inhibitors and then evaluated RBC shapes as above (Fig. S7*A*). Inhibition of Rho kinase with Y-27632 (47) at 5 μM and 20 μM caused a loss in RBC biconcavity similar to that seen in blebbistatin-treated RBCs after both 30 min and 2 h of

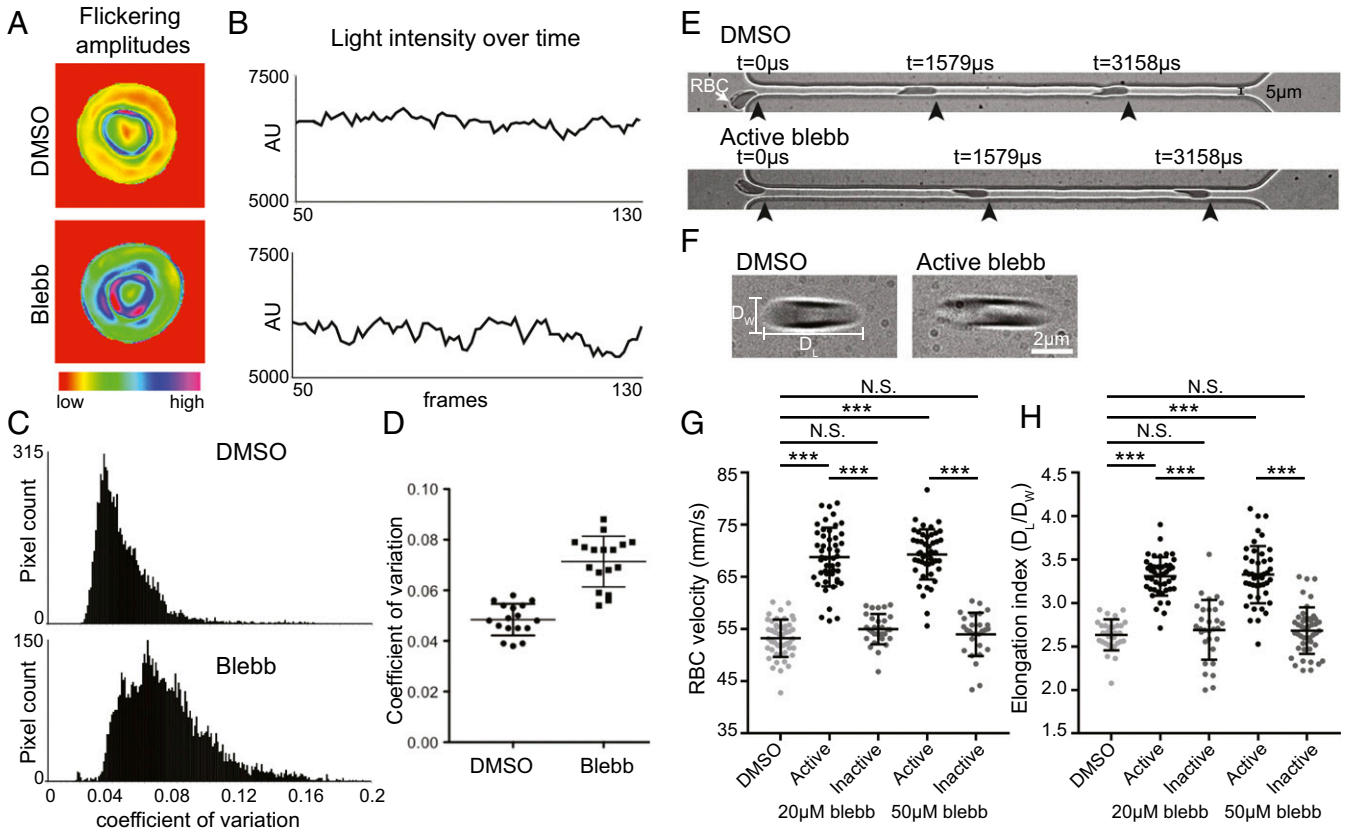

Fig. 5. NMIIA motor activity controls the amplitude and variability of RBC membrane flickering and RBC deformability during flow in microchannels. (*A–D*) Human RBCs were treated with 5 μM blebbistatin or DMSO. (*A*) Color-coded representations of whole-RBC flickering amplitudes in representative cells, where red represents amplitude changes near zero and purple represents maximum changes. The blebbistatin-treated cell has higher flickering amplitudes throughout the cell. (*B*) Changes in light intensity over time in an area of 3 × 3 pixels in representative cells, as recorded by phase-contrast microscopy. The area from the blebbistatin-treated cell has larger changes in light intensity. (*C*) Frequency distributions of the coefficients of variation in all pixel amplitudes from representative cells. The blebbistatin-treated cell has more pixels with high coefficients of variation. (*D*) Coefficients of variation of membrane flickering amplitudes ($n = 15$ RBCs per treatment condition). (*E* and *G*) Treatment with active blebbistatin, but not inactive blebbistatin or DMSO, increases the velocity of RBCs flowing through a 5-μm-wide channel, corresponding to an increase in deformability. Representative cells are shown in *E*. Cells from two to three individual donors (***$P < 0.0001$) are shown in *G*: DMSO ($n = 48$), 20 μM active blebbistatin ($n = 48$), 20 μM inactive blebbistatin ($n = 30$), 50 μM active blebbistatin ($n = 47$), and 50 μM inactive blebbistatin ($n = 28$). Data are presented as mean ± SD for each condition. (*F* and *H*) Treatment with active, but not inactive, blebbistatin or DMSO increases the shear-induced elongation index as RBCs flow through a 20-μm-wide constriction in a 30-μm-wide channel, corresponding to an increase in deformability. Representative cells are shown in *F*. Cells from two to three individual donors (***$P < 0.0001$) are shown in *H*: DMSO ($n = 30$), 20 μM active blebbistatin ($n = 45$), 20 μM inactive blebbistatin ($n = 30$), 50 μM active blebbistatin ($n = 45$), 50 μM inactive blebbistatin ($n = 45$). Data are presented as mean ± SD for each condition.

treatment (Fig. S7*C*). Treatment with 20 μM Y-27632 also increased RBC aspect ratios after 2 h of treatment, although to a smaller extent than seen after blebbistatin treatment (Fig. S7*B*). By contrast, inhibition of MLCK with 5 μM Peptide 18 (P18) (48) did not affect RBC biconcavity or aspect ratios, even after 2 h of treatment (Fig. S7 *D* and *E*). These data suggest that Rho kinase, but not MLCK, phosphorylates the NMIIA RLC to control RBC shape.

NMIIA Motor Activity Controls RBC Membrane Deformability. Given that NMIIA motor activity controls RBC morphology, we predicted that NMIIA contractility maintains membrane curvature by promoting membrane tension and reducing local membrane deformability. Nanoscale, ATP-dependent membrane oscillations of variable frequency observed in RBCs and other cell types are a sensitive measure of local membrane deformability (49–53). We observed these oscillations by filming changes in light scattering at the RBC surface using positive low-phase-contrast microscopy. Inhibition of NMIIA activity with blebbistatin increased the magnitude (Fig. 5 *A* and *B*) and coefficient of variation (Fig. 5 *C* and *D*) of oscillation amplitudes. This suggests that, in untreated RBCs, NMIIA contractility dampens spontaneous membrane oscillations and reduces local membrane deformability.

Global RBC deformability during transit through blood vessels in vivo depends on RBC biconcave shape and local membrane deformability (2, 3). We evaluated global RBC deformability ex vivo by measuring rates of RBC flow through a microfluidic device with a 5-μm channel, narrower than the 8-μm diameter of human RBCs (54) (Fig. 5*E*). RBCs treated with 20 μM and 50 μM active blebbistatin traveled through the channel more rapidly than DMSO- and inactive blebbistatin-treated control RBCs (Fig. 5*G*). RBCs treated with 20 μM and 50 μM active blebbistatin also displayed greater shear-induced elongation as they passed through a wide (20 μm) constriction in a 30-μm channel (Fig. 5 *F* and *H*). Blebbistatin treatment did not affect increases in RBC flow through narrow microchannels or RBC shear-induced elongation in response to decreases in oxygen pressure (PO_2) (Fig. S8). We conclude that, in untreated RBCs, NMIIA motor activity promotes membrane tension to control local and global RBC deformability.

Discussion

The membrane skeleton, a long-range, 2D, periodic network of short F-actins cross-linked by flexible spectrin molecules, underlies the plasma membrane of metazoan cells, including RBCs. Here, we identified NMIIA contractility as a mechanism controlling

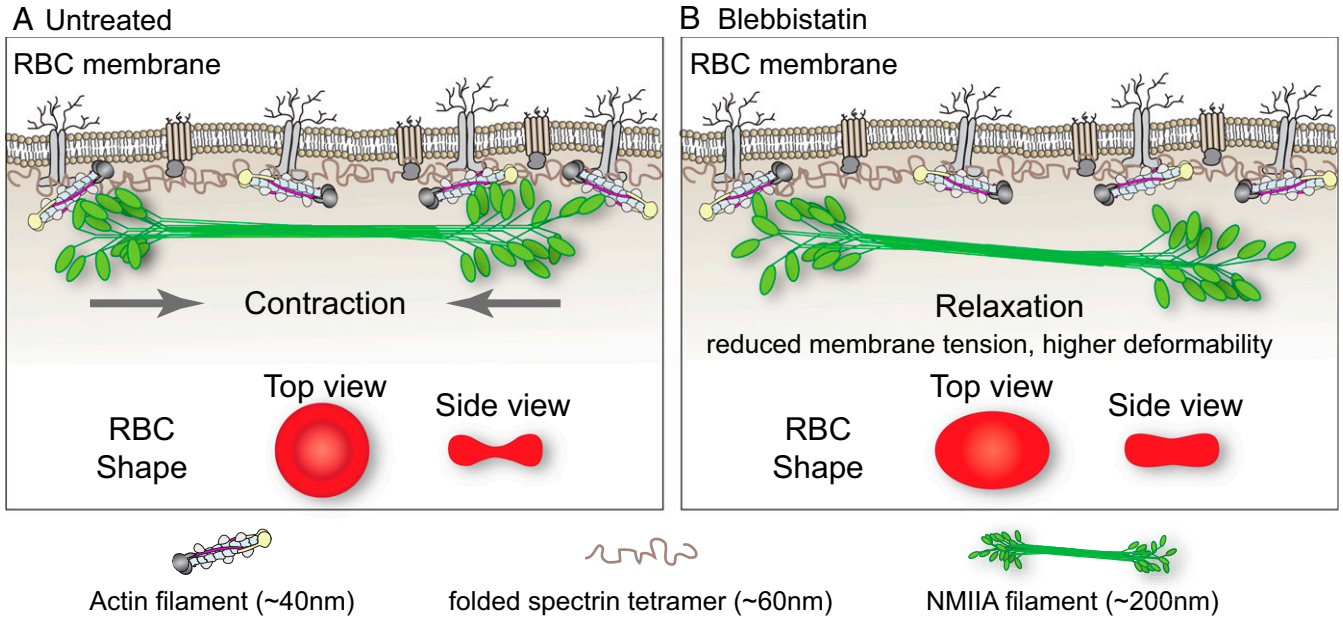

Fig. 6. Model for NMIIA contractility in the spectrin–F-actin network and its effect on RBC membrane morphology and mechanical properties. (*A*) Two-dimensional network of long, flexible spectrin tetramers that cross-link short actin filaments (the spectrin–F-actin network) is attached to the plasma membrane (not drawn to scale) via associations of network components with transmembrane proteins. NMIIA bipolar filaments can associate with the short F-actins of the spectrin–F-actin network via their motor domains. Through these interactions, NMIIA contractile forces (arrows) could promote membrane tension in the spectrin–F-actin network to maintain normal biconcave RBC shapes, as shown in top and side views (red RBCs), and to control RBC deformability. The NMIIA filament depicted in this diagram is ~200 nm long, but our data and other studies show that myosin filaments can be up to 450 nm long in cells. This would double the length scale over which one NMIIA filament could generate contractile forces on the membrane. (*B*) Blebbistatin treatment weakens the association between NMIIA motor domains and F-actin, causing NMIIA filaments to partially or completely dissociate from the spectrin–F-actin network. This dissociation would lead to a relaxation of the contractile forces on the network, reducing membrane tension and increasing deformability. This relaxation leads to an elongation of RBC shape, as shown in the top view, and a decrease of biconcavity, as shown in the side view (red RBCs). As indicated in the legend below the figure, the F-actin barbed ends are capped by adducin (yellow) and F-actin pointed ends are capped by tropomodulin (dark gray), with tropomyosin rods (purple) spanning their length and protein 4.1R (tan) at the spectrin–F-actin interaction sites (5). Spectrin tetramers are depicted in the folded conformation (40–70 nm) of the native, unspread membrane skeleton, but are able to unfold and extend to nearly 200 nm in length (5, 7).

RBC biconcave shape and deformability. Data from fluorescence microscopy, as well as biochemical and biophysical approaches, lead us to propose that NMIIA forms bipolar filaments that exert contractile forces via binding of their motor domains to the short F-actins in the membrane skeleton (Fig. 6*A*). In support of this conclusion, inhibition of NMIIA contractile activity with blebbistatin reduces the association of NMIIA with F-actin at the membrane, as indicated schematically in Fig. 6*B*, disrupting the RBC biconcave disk shape and increasing RBC deformability.

NMIIA bipolar filaments likely exert force on a small subset of RBC F-actins, since NMIIA puncta have a low density at the membrane (0.5 puncta per square micrometer) compared with ~250 F-actins per square micrometer (5, 6). Also, blebbistatin-induced NMIIA dissociation from the membrane does not result in detectable changes in F-actin distribution by Western blotting and TIRF imaging. Therefore, we hypothesize that NMIIA acts as a dynamic cross-linker between short F-actins, constrained by their linkages in the spectrin–F-actin network (Fig. 6*A*), rather than by inducing large-scale F-actin translocation and/or network rearrangements. NMIIA/F-actin cross-linking activity in the membrane skeleton may be a conserved mechanism for actomyosin regulation of membrane tension, curvature, cell shape, and biomechanics.

Our mRNA and protein expression analyses confirm and extend previous studies, which show that immature erythroid progenitors express both the NMIIA and NMIIB HC isoforms (27–29). Expression of both isoforms decreases during later stages of terminal erythroid maturation, in agreement with recent proteomics studies (55–58), but NMIIA becomes the predominant isoform in mature RBCs. While some proteomics studies also identify NMIIB in mature RBCs (56, 57), this apparent disagreement with our Western blot data could result from increased sensitivity of mass spectrometry and/or leukocyte contamination.

Our analysis of superresolution fluorescence microscopy images reveals ~150 NMIIA motor domain puncta per RBC, and NMIIA bipolar filaments can be identified by colabeling of the motor and tail domains. Based on previous biochemical analysis estimating that each RBC contains ~6,200 NMII monomers that could form ~210 bipolar filaments of 30 monomers each (15), this indicates that a significant fraction of RBC NMIIA may form bipolar filaments. The inability of previous electron microscopy studies to detect NMII bipolar filaments, in either intact RBCs or ghosts, is likely due to the high concentration of electron-dense hemoglobin and the high density of the spectrin–F-actin network at the membrane, together with the low density of bipolar NMIIA filaments. In addition, common ghost preparation conditions, such as use of lysis buffers without Mg^{2+} or dialysis into very low ionic strength buffers during expansion of the membrane skeleton (59–61), disrupt interactions between NMIIA and F-actin (15, 62).

Our analysis of NMIIA/F-actin interactions suggests that this association is mediated by NMIIA motor domains binding to membrane skeleton F-actin. As originally observed for *Dictyostelium discoideum* NMII association with the membrane (62), MgATP reduces RBC NMIIA cosedimentation with the Triton-insoluble membrane skeleton several-fold. By contrast, spectrin, F-actin, and other membrane skeleton components exclusively associate with the membrane skeleton in the presence and absence of MgATP. Treatment of RBCs with blebbistatin, which maintains myosin motor domains in a weak F-actin binding conformation (43), also decreases the amount of NMIIA associated with the membrane, as assessed by TIRF microscopy.

Phosphorylation of the RBC NMIIA HC and RLC suggests that a significant fraction of RBC NMIIA is active and competent for filament assembly, while reduced HC phosphorylation indicates increased stability of membrane skeleton-associated NMIIA. However, the upstream signaling pathways that may activate or inhibit HC and RLC phosphorylation in RBCs remain poorly understood. RBCs contain Rho/Rho-kinase pathway components that could phosphorylate the RLC (63), and Rho kinase inhibition with Y-27632 leads to a similar, although less pronounced, RBC shape change and increase in deformability (64) compared with blebbistatin-treated RBCs. While blebbistatin specifically inhibits NMII motor activity, it is possible that the effects of Y-27632 are mediated by a Rho kinase target in addition to or other than the NMIIA RLC, such as adducin [which caps RBC membrane skeleton F-actins and promotes spectrin–F-actin binding (65–67)], or by an alternative signaling pathway.

Inhibition of MLCK with P18 does not affect either RBC aspect ratio or biconcavity. This suggests that MLCK may not contribute significantly to the regulation of RBC NMIIA contractility by RLC phosphorylation. Proteomic studies indicate that RBCs also contain casein kinase and protein kinase C, which can phosphorylate either the NMII RLC or the C terminus of the HC (22–24, 46) and may play a role in regulating RBC NMIIA activity. Alternatively, a portion of the phosphorylated RLC may be protected from turnover by RLC phosphatases. In this case, sufficient NMIIA may remain stably phosphorylated and competent to assemble into bipolar filaments and interact with membrane skeleton F-actin to generate tension and control RBC shape. In support of this conclusion, RBCs do not undergo the regulated, dynamic, global F-actin rearrangements seen in migrating cells (68), suggesting that RBCs may also have lower levels of RLC phosphorylation-regulated turnover of NMIIA bipolar filaments.

Other F-actin–binding proteins could also modulate RBC NMIIA activity. Tropomyosin isoforms regulate the F-actin–activated MgATPase and F-actin sliding velocity of NMIIA and other myosin isoforms (69–71). RBCs contain two tropomyosins, Tpm3.1 and Tpm1.9, present in equimolar amounts and extending along the length of each short F-actin in the membrane skeleton (5, 72–74). RBCs also contain caldesmon (two caldesmons per short F-actin), which, together with tropomyosin, regulates F-actin–activated myosin ATPase activity in vitro (5, 19). A Tpm3.1-deficient mouse in which RBCs have abnormal shapes and deformability (75) will provide an opportunity to test whether Tpm3.1 regulates NMIIA in RBCs in vivo.

Inhibition of NMIIA motor activity with blebbistatin leads to an increase in variance, as well as mean values, for RBC aspect ratio and degree of biconcavity, suggesting cell-to-cell variability in dependence on NMIIA contractility to control RBC shape. This may result from changes in membrane skeleton mechanical properties during RBC aging in the circulation (50, 76, 77). Human and mouse RBCs with mutations in integral membrane skeleton proteins have more dramatic shape changes than those observed in blebbistatin-treated RBCs. Mutations that disrupt spectrin–F-actin linkages lead to highly elongated RBCs (elliptocytes), while mutations that disrupt network-membrane attachments lead to rounder RBCs with loss of membrane surface area (spherocytes) (2, 78). This difference in magnitude of the phenotype further supports our conclusion that NMIIA is not an integral component of the membrane skeleton but associates with the spectrin–F-actin network in a dynamic and transient manner.

In endothelial cells migrating in 3D collagen gels, NMII contractility is associated with regions of negative plasma membrane curvature (79), which is analogous to the central region (dimple) of the biconcave RBC. Although we do not detect selective enrichment of NMIIA in the dimple region (or at the rim), it is possible that activated NMIIA with phosphorylated RLC could be differentially localized to the dimple or rim. Alternatively, NMIIA contractility distributed across the entire membrane may maintain global tension in the spectrin–F-actin network, which couples to the membrane bilayer, to promote membrane flattening and dimple formation. To date, theoretical models for RBC biconcave shape (2, 80) have not considered an active role for myosin-based contractility in generating membrane tension.

In addition to maintenance of RBC biconcave shape, blebbistatin treatments indicate that NMIIA contractility normally dampens spontaneous membrane flickering. Depletion of MgATP reduces membrane flickering (49, 51–53), which could be due to further dampening by increased NMIIA/F-actin binding in these conditions. As NMIIA contractility also controls global RBC deformability and shear-induced elongation during flow, NMIIA/F-actin cross-linking activity may be important for the ability of the spectrin–F-actin membrane skeleton to enhance RBC resilience and preserve biconcave disk shapes.

RBC membrane flickering and transit through narrow channels also depend on F-actin assembly (49, 68), suggesting NMIIA contractility and F-actin polymerization may synergistically modulate membrane mechanical properties in RBCs. Shear-induced deformation causes Ca^{2+} influx into RBCs through Piezo1 or other mechanosensitive channels (81, 82), which could influence NMIIA motor activity and F-actin polymerization to control membrane tension. Future studies will investigate the role of NMIIA in RBC circulatory function in vivo and determine the importance of NMIIA and other NMII isoforms for the functions of spectrin–F-actin networks in membrane morphology and mechanical resilience in other cell types.

Materials and Methods

Experimental procedures for culturing human $CD34^+$ cells, flow cytometry, and qRT-PCR; immunofluorescence labeling of NMIIA and phalloidin labeling of F-actin in RBCs; AiryScan and TIRF microscopy and image analysis; RBC isolation and biochemical procedures; blebbistatin, P18, and Y-27632 treatment of RBCs; confocal microscopy and 3D shape measurements; membrane flickering; and microfluidics assays are described in *SI Materials and Methods*. All experiments with human RBCs were approved by the Institutional Review Board at The Scripps Research Institute, Northwell Health System, Beth Israel Deaconess Medical Center, or the Rochester Institute of Technology. All study participants provided informed consent.

ACKNOWLEDGMENTS. We thank Connie Smith and Ilan Wittstein for helping V.M.F. with the initial biochemical experiments. We thank Kasturi Pal for help with additional biochemical experiments and the other members of the V.M.F. laboratory for helpful suggestions and comments. This work was supported by a grant from the Whitaker Foundation (to V.M.F.); NIH Grants GM34225 and HL083464 (to V.M.F.), Grant HL134043 (subcontract to L.B.), and Grant HL126497 (to I.C.G.); and National Science Foundation Award CBET-1560709 (to J.W.). A.S.S. was supported by NIH/National Center for Advancing Translational Sciences Clinical and Translational Science Award UL1 TR001114 to the Scripps Translational Science Institute. L.B. is the recipient of an Allied World St. Baldrick's Scholar Award.

1. Mohandas N, Evans E (1994) Mechanical properties of the red cell membrane in relation to molecular structure and genetic defects. *Annu Rev Biophys Biomol Struct* 23:787–818.
2. Mohandas N, Gallagher PG (2008) Red cell membrane: Past, present, and future. *Blood* 112:3939–3948.
3. Chien S (1987) Red cell deformability and its relevance to blood flow. *Annu Rev Physiol* 49:177–192.
4. Forsyth AM, Wan J, Owrutsky PD, Abkarian M, Stone HA (2011) Multiscale approach to link red blood cell dynamics, shear viscosity, and ATP release. *Proc Natl Acad Sci USA* 108:10986–10991.
5. Fowler VM (2013) The human erythrocyte plasma membrane: A Rosetta Stone for decoding membrane-cytoskeleton structure. *Curr Top Membr* 72:39–88.
6. Gokhin DS, Fowler VM (2016) Feisty filaments: Actin dynamics in the red blood cell membrane skeleton. *Curr Opin Hematol* 23:206–214.
7. Discher DE (2000) New insights into erythrocyte membrane organization and microelasticity. *Curr Opin Hematol* 7:117–122.
8. Bennett V, Lorenzo DN (2013) Spectrin- and ankyrin-based membrane domains and the evolution of vertebrates. *Curr Top Membr* 72:1–37.
9. Bennett V, Lorenzo DN (2016) An adaptable spectrin/ankyrin-based mechanism for long-range organization of plasma membranes in vertebrate tissues. *Curr Top Membr* 77:143–184.

10. Machnicka B, et al. (2014) Spectrins: A structural platform for stabilization and activation of membrane channels, receptors and transporters. *Biochim Biophys Acta* 1838:620–634.
11. Hodgkin T, Lister JJ (1827) Notice of some microscopic observations of the blood and animal tissues. *Philoso Mag* 2:130–138.
12. Lux SE, 4th (2016) Anatomy of the red cell membrane skeleton: Unanswered questions. *Blood* 127:187–199.
13. Hoffman JF (2001) Questions for red blood cell physiologists to ponder in this millenium. *Blood Cells Mol Dis* 27:57–61.
14. Wong AJ, Kiehart DP, Pollard TD (1985) Myosin from human erythrocytes. *J Biol Chem* 260:46–49.
15. Fowler VM, Davis JQ, Bennett V (1985) Human erythrocyte myosin: Identification and purification. *J Cell Biol* 100:47–55.
16. Higashihara M, Hartshorne DJ, Craig R, Ikebe M (1989) Correlation of enzymatic properties and conformation of bovine erythrocyte myosin. *Biochemistry* 28: 1642–1649.
17. Colin FC, Schrier SL (1991) Myosin content and distribution in human neonatal erythrocytes are different from adult erythrocytes. *Blood* 78:3052–3055.
18. Fowler VM (1986) An actomyosin contractile mechanism for erythrocyte shape transformations. *J Cell Biochem* 31:1–9.
19. der Terrossian E, Deprette C, Lebbar I, Cassoly R (1994) Purification and characterization of erythrocyte caldesmon. Hypothesis for an actin-linked regulation of a contractile activity in the red blood cell membrane. *Eur J Biochem* 219:503–511.
20. Cibert C, Prulière G, Lacombe C, Deprette C, Cassoly R (1999) Calculation of a gap restoration in the membrane skeleton of the red blood cell: Possible role for myosin II in local repair. *Biophys J* 76:1153–1165.
21. Salbreux G, Charras G, Paluch E (2012) Actin cortex mechanics and cellular morphogenesis. *Trends Cell Biol* 22:536–545.
22. Vicente-Manzanares M, Ma X, Adelstein RS, Horwitz AR (2009) Non-muscle myosin II takes centre stage in cell adhesion and migration. *Nat Rev Mol Cell Biol* 10:778–790.
23. Heissler SM, Manstein DJ (2013) Nonmuscle myosin-2: Mix and match. *Cell Mol Life Sci* 70:1–21.
24. Conti MA, Adelstein RS (2008) Nonmuscle myosin II moves in new directions. *J Cell Sci* 121:11–18.
25. Schiffhauer ES, Robinson DN (2017) Mechanochemical signaling directs cell-shape change. *Biophys J* 112:207–214.
26. Ma X, et al. (2010) Ablation of nonmuscle myosin II-B and II-C reveals a role for nonmuscle myosin II in cardiac myocyte karyokinesis. *Mol Biol Cell* 21:3952–3962.
27. Merryweather-Clarke AT, et al. (2011) Global gene expression analysis of human erythroid progenitors. *Blood* 117:e96–e108.
28. An X, et al. (2014) Global transcriptome analyses of human and murine terminal erythroid differentiation. *Blood* 123:3466–3477.
29. Ubukawa K, et al. (2012) Enucleation of human erythroblasts involves non-muscle myosin IIB. *Blood* 119:1036–1044.
30. Sega MF, Chu H, Christian JA, Low PS (2015) Fluorescence assay of the interaction between hemoglobin and the cytoplasmic domain of erythrocyte membrane band 3. *Blood Cells Mol Dis* 55:266–271.
31. Diez-Silva M, Dao M, Han J, Lim CT, Suresh S (2010) Shape and biomechanical characteristics of human red blood cells in health and disease. *MRS Bull* 35:382–388.
32. Huff J (2015) The airyscan detector from ZEISS: Confocal imaging with improved signal-to-noise ratio and super-resolution. *Nat Methods* 12.
33. Ebrahim S, et al. (2013) NMII forms a contractile transcellular sarcomeric network to regulate apical cell junctions and tissue geometry. *Curr Biol* 23:731–736.
34. Billington N, Wang A, Mao J, Adelstein RS, Sellers JR (2013) Characterization of three full-length human nonmuscle myosin II paralogs. *J Biol Chem* 288:33398–33410.
35. Beach JR, et al. (2014) Nonmuscle myosin II isoforms coassemble in living cells. *Curr Biol* 24:1160–1166.
36. Shutova MS, Spessott WA, Giraudo CG, Svitkina T (2014) Endogenous species of mammalian nonmuscle myosin IIA and IIB include activated monomers and heteropolymers. *Curr Biol* 24:1958–1968.
37. Fenix AM, et al. (2016) Expansion and concatenation of non-muscle myosin IIA filaments drive cellular contractile system formation during interphase and mitosis. *Mol Biol Cell* 27:1465–1478.
38. Beach JR, et al. (2017) Actin dynamics and competition for myosin monomer govern the sequential amplification of myosin filaments. *Nat Cell Biol* 19:85–93.
39. Zhang Y, et al. (2012) Mouse models of MYH9-related disease: Mutations in nonmuscle myosin II-A. *Blood* 119:238–250.
40. Lehtimäki JI, et al. (2017) UNC-45a promotes myosin folding and stress fiber assembly. *J Cell Biol* 216:4053–4072.
41. Mattheyses AL, Simon SM, Rappoport JZ (2010) Imaging with total internal reflection fluorescence microscopy for the cell biologist. *J Cell Sci* 123:3621–3628.
42. Korpman RA, Dorrough DC, Brailsford JD, Bull BS (1978) The red cell shape as an indicator of membrane structure: Ponder's rule reexamined. *Red Cell Rheology*, eds Bessis M, Shohet SB, Mohandas N (Springer, Berlin), pp 311–330.
43. Kovács M, Tóth J, Hetényi C, Málnási-Csizmadia A, Sellers JR (2004) Mechanism of blebbistatin inhibition of myosin II. *J Biol Chem* 279:35557–35563.
44. Yu J, Fischman DA, Steck TL (1973) Selective solubilization of proteins and phospholipids from red blood cell membranes by nonionic detergents. *J Supramol Struct* 1: 233–248.
45. Moyer JD, et al. (2010) Tropomodulin 1-null mice have a mild spherocytic elliptocytosis with appearance of tropomodulin 3 in red blood cells and disruption of the membrane skeleton. *Blood* 116:2590–2599.
46. Dulyaninova NG, Bresnick AR (2013) The heavy chain has its day: Regulation of myosin-II assembly. *Bioarchitecture* 3:77–85.
47. Ishizaki T, et al. (2000) Pharmacological properties of Y-27632, a specific inhibitor of rho-associated kinases. *Mol Pharmacol* 57:976–983.
48. Lukas TJ, Mirzoeva S, Slomczynska U, Watterson DM (1999) Identification of novel classes of protein kinase inhibitors using combinatorial peptide chemistry based on functional genomics knowledge. *J Med Chem* 42:910–919.
49. Tuvia S, Levin S, Bitler A, Korenstein R (1998) Mechanical fluctuations of the membrane-skeleton are dependent on F-actin ATPase in human erythrocytes. *J Cell Biol* 141:1551–1561.
50. Costa M, Ghiran I, Peng CK, Nicholson-Weller A, Goldberger AL (2008) Complex dynamics of human red blood cell flickering: Alterations with in vivo aging. *Phys Rev E Stat Nonlin Soft Matter Phys* 78:020901.
51. Betz T, Lenz M, Joanny JF, Sykes C (2009) ATP-dependent mechanics of red blood cells. *Proc Natl Acad Sci USA* 106:15320–15325.
52. Park Y, et al. (2010) Metabolic remodeling of the human red blood cell membrane. *Proc Natl Acad Sci USA* 107:1289–1294.
53. Rodríguez-García R, et al. (2015) Direct cytoskeleton forces cause membrane softening in red blood cells. *Biophys J* 108:2794–2806.
54. Wan J, Forsyth AM, Stone HA (2011) Red blood cell dynamics: From cell deformation to ATP release. *Integr Biol* 3:972–981.
55. Basu A, et al. (2015) Proteome analysis of the triton-insoluble erythrocyte membrane skeleton. *J Proteomics* 128:298–305.
56. Wilson MC, et al. (2016) Comparison of the proteome of adult and cord erythroid cells, and changes in the proteome following reticulocyte maturation. *Mol Cell Proteomics* 15:1938–1946.
57. Bryk AH, Wiśniewski JR (2017) Quantitative analysis of human red blood cell proteome. *J Proteome Res* 16:2752–2761.
58. Gautier EF, et al. (2016) Comprehensive proteomic analysis of human erythropoiesis. *Cell Rep* 16:1470–1484.
59. Byers TJ, Branton D (1985) Visualization of the protein associations in the erythrocyte membrane skeleton. *Proc Natl Acad Sci USA* 82:6153–6157.
60. Shen BW, Josephs R, Steck TL (1986) Ultrastructure of the intact skeleton of the human erythrocyte membrane. *J Cell Biol* 102:997–1006.
61. Liu SC, Derick LH, Palek J (1987) Visualization of the hexagonal lattice in the erythrocyte membrane skeleton. *J Cell Biol* 104:527–536.
62. Spudich JA (1974) Biochemical and structural studies of actomyosin-like proteins from non-muscle cells. II. Purification, properties, and membrane association of actin from amoebae of Dictyostelium discoideum. *J Biol Chem* 249:6013–6020.
63. Tiftik RN, Başkurt OK, Kul S, Büyükafşar K (2014) The functional significance of the rho/rho-kinase pathway in human erythrocytes. *Turk J Haematol* 31:168–174.
64. Thuet KM, Bowles EA, Ellsworth ML, Sprague RS, Stephenson AH (2011) The Rho kinase inhibitor Y-27632 increases erythrocyte deformability and low oxygen tension-induced ATP release. *Am J Physiol Heart Circ Physiol* 301:H1891–H1896.
65. Kimura K, et al. (1998) Regulation of the association of adducin with actin filaments by Rho-associated kinase (Rho-kinase) and myosin phosphatase. *J Biol Chem* 273: 5542–5548.
66. Fukata Y, Oshiro N, Kaibuchi K (1999) Activation of moesin and adducin by Rho-kinase downstream of Rho. *Biophys Chem* 82:139–147.
67. Anong WA, et al. (2009) Adducin forms a bridge between the erythrocyte membrane and its cytoskeleton and regulates membrane cohesion. *Blood* 114:1904–1912.
68. Gokhin DS, et al. (2015) Dynamic actin filaments control the mechanical behavior of the human red blood cell membrane. *Mol Biol Cell* 26:1699–1710.
69. Barua B, Nagy A, Sellers JR, Hitchcock-DeGregori SE (2014) Regulation of nonmuscle myosin II by tropomyosin. *Biochemistry* 53:4015–4024.
70. Manstein DJ, Mulvihill DP (2016) Tropomyosin-mediated regulation of cytoplasmic myosins. *Traffic* 17:872–877.
71. Pathan-Chhatbar S, et al. (2018) Three mammalian tropomyosin isoforms have different regulatory effects on nonmuscle myosin-2B and filamentous β-actin in vitro. *J Biol Chem* 293:863–875.
72. Fowler VM, Bennett V (1984) Erythrocyte membrane tropomyosin. Purification and properties. *J Biol Chem* 259:5978–5989.
73. Sung LA, Lin JJ (1994) Erythrocyte tropomodulin binds to the N-terminus of hTM5, a tropomyosin isoform encoded by the gamma-tropomyosin gene. *Biochem Biophys Res Commun* 201:627–634.
74. Sung LA, et al. (2000) Tropomyosin isoform 5b is expressed in human erythrocytes: Implications of tropomodulin-TM5 or tropomodulin-TM5b complexes in the protofilament and hexagonal organization of membrane skeletons. *Blood* 95:1473–1480.
75. Sui Z, et al. (2017) Stabilization of F-actin by tropomyosin isoforms regulates the morphology and mechanical behavior of red blood cells. *Mol Biol Cell* 28:2531–2542.
76. Sutera SP, et al. (1985) Age-related changes in deformability of human erythrocytes. *Blood* 65:275–282.
77. Huang YX, et al. (2011) Human red blood cell aging: Correlative changes in surface charge and cell properties. *J Cell Mol Med* 15:2634–2642.
78. Da Costa L, Galimand J, Fenneteau O, Mohandas N (2013) Hereditary spherocytosis, elliptocytosis, and other red cell membrane disorders. *Blood Rev* 27:167–178.
79. Elliott H, et al. (2015) Myosin II controls cellular branching morphogenesis and migration in three dimensions by minimizing cell-surface curvature. *Nat Cell Biol* 17: 137–147.
80. Steck TL (1989) Red cell shape. *Cell Shape: Determinants, Regulation, and Regulatory Role* (Academic, San Diego), pp 205–246.
81. Cahalan SM, et al. (2015) Piezo1 links mechanical forces to red blood cell volume. *eLife* 4:e07370.
82. Cinar E, et al. (2015) Piezo1 regulates mechanotransductive release of ATP from human RBCs. *Proc Natl Acad Sci USA* 112:11783–11788.